



PCCP

**Does Boron or Nitrogen Substitution Affect Hydrogen  
Physisorption on Open Carbon Surfaces?**

Journal:	<i>Physical Chemistry Chemical Physics</i>
Manuscript ID	CP-COM-08-2022-003975.R1
Article Type:	Communication
Date Submitted by the Author:	11-Nov-2022
Complete List of Authors:	Rowsey, Rylan; Montana State University, Department of Chemistry and Biochemistry Taylor, Erin; Montana State University, Department of Chemistry and Biochemistry Hinson, Ryan; Montana State University, Department of Chemistry and Biochemistry Compton, Dalton; Montana State University, Department of Chemistry and Biochemistry Stadie, Nicholas; Montana State University, Department of Chemistry and Biochemistry Szilagy, Robert; The University of British Columbia Okanagan, Chemistry

SCHOLARONE™  
Manuscripts

## COMMUNICATION

## Does Boron or Nitrogen Substitution Affect Hydrogen Physisorption on Open Carbon Surfaces?

Received 00th January 20xx,  
Accepted 00th January 20xx

Rylan Rowsey,<sup>a</sup> Erin E. Taylor,<sup>a</sup> Ryan W. Hinson,<sup>a</sup> Dalton Compton,<sup>a</sup> Nicholas P. Stadie,<sup>a\*</sup> and Robert K. Szilagyi<sup>b\*</sup>

DOI: 10.1039/x0xx00000x

**Incorporation of heteroatoms in carbon materials is commonly expected to influence their physical or chemical properties. However, contrary to previous results for methane adsorption, no technologically significant effect was identified for the hydrogen physisorption energies (measured 4.1–4.6 kJ mol<sup>-1</sup> and calculated  $q_{st} = \Delta H_{ads} = 4.1 \pm 0.7$  kJ mol<sup>-1</sup> using a comprehensive set of levels of theory) as a function of B- and N-substitution of a mid-plane C-site on open carbon surfaces.**

The adsorption of hydrogen on carbon-based surfaces has important implications in a plethora of energy storage and conversion systems from fuel-cell electrodes to high surface area adsorbents.<sup>1, 2</sup> Consequently, the quantitative evaluation of H<sub>2</sub> binding has been the focus of numerous experimental (Table S1) and theoretical studies (Table S2). Experimental H<sub>2</sub> physisorption energies vary from 4–8 kJ mol<sup>-1</sup> on carbonaceous adsorbents and on MOFs.<sup>3–9</sup> H<sub>2</sub> physisorption on “doped” porous carbons is still not conclusively understood. The simplest substitutional dopants are boron and nitrogen; each introduces an electron hole or an extra electron into the carbon framework, respectively. Boron substitution has been reported to either enhance<sup>12–14</sup> or have no effect<sup>7</sup> on H<sub>2</sub> physisorption. Similarly, nitrogen substitution has also been claimed to either enhance<sup>6</sup> or have no influence<sup>12</sup> on H<sub>2</sub> binding. This ambiguity is (at least partly) due to the experimental error that is notoriously pervasive in H<sub>2</sub> adsorption measurements.<sup>16</sup> The challenges of resolving the influence of B- and N-doping is further complicated by the often overlapping effects of other heteroatoms (O

substitutions), the variety of possible chemical environments (acid/base, H-bonding, dipoles), and pore size or geometry effects.

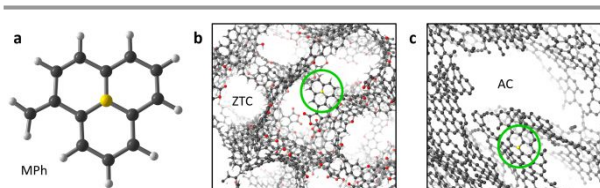
Computational studies employing a range of different porous carbon models from benzene, pyrene, coronene, graphene fragments, and carbon nanotubes, to periodic slit pore models report binding energies in agreement with experiments for H<sub>2</sub> on unsubstituted porous carbon surfaces (5–10 kJ mol<sup>-1</sup>, Table S2).<sup>17–23</sup> To date, no computational study has emerged that directly compares H<sub>2</sub> physisorption on unsubstituted, B-, and N-substituted open carbon surface models at an accuracy that is technologically impactful. Comparative studies reveal a large degree of uncertainty about which substitution (B,<sup>22</sup> none,<sup>20</sup> or N<sup>24</sup>) shows enhancement in physisorption. This is further compounded by limitations owing to considering chemisorption<sup>25–27</sup> and confinement between graphitic layers.<sup>28, 29</sup>

Our recent work<sup>30</sup> demonstrates that CH<sub>4</sub> physisorption on open carbon surfaces is in fact sensitive to the nature of heteroatom substitution. The estimated effect is large enough to have technological relevance for natural gas storage. In the present work, on the other hand, no technologically relevant effect was observed for the presence of B- or N-substitution toward H<sub>2</sub> storage at ambient or sub-ambient temperatures. Employing physisorption models with 3 compositions and up to 6 H<sub>2</sub> molecules in 35 arrangements, this study places a strong emphasis on systematic modelling in order to avoid the pitfalls of exaggerating the impact of heteroatom doping in applications.<sup>31</sup> The observations we made for a small adsorbent model were expanded by considering molecular

<sup>a</sup> Department of Chemistry & Biochemistry, Montana State University, Bozeman, MT 59717, United States of America

<sup>b</sup> Department of Chemistry, University of British Columbia – Okanagan, Kelowna, BC V1V 1V7, Canada

† Corresponding authors: nstadie@montana.edu and robert.szilagyi@ubc.ca. Electronic Supplementary Information (ESI) available: Literature review of experimental and theoretical H<sub>2</sub> adsorption energies, details of the computational model and methods used herein, geometric structure analysis of all H<sub>2</sub> adsorption models, H<sub>2</sub> dissociation energies from DFT and correlated MO calculations, and experimental isosteric heat as a function of H<sub>2</sub> loading. See DOI: 10.1039/x0xx00000x. Atomic positional coordinates, electron density cube files, and other significant details of the computational studies are also provided at a Zenodo depository: DOI: 10.5281/zenodo.4330760.



**Scheme 1.** Methyldiene phenalene (a, MPh): a molecular maquette of porous carbon surfaces such as (b) zeolite-templated carbon (ZTC<sup>10</sup>) and (c) activated carbon (AC<sup>11</sup>).

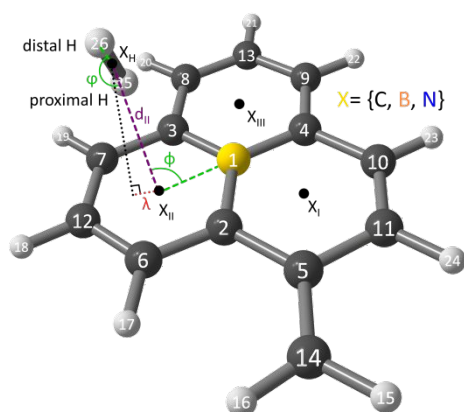


**Figure 1.** Internal coordinates describing the physisorption interaction of  $H_2$  with MPh: distance of adsorption ( $d$ ,  $d_{ii}$  is shown above Ring II), directionality of adsorption ( $\varphi$ , end- or side-on arrangement), angle of adsorption ( $\phi$ , off-centeredness), and displacement with respect to the nearest ring centroid ( $\lambda$ ). Z-matrix definitions for end-on (as shown here) and side-on  $H_2$  orientation are given in Table S3. Potential energy surface scans of the  $H_2$  approach are presented in Figures S1-S2.

maquettes of larger size and even embedded in liquid  $H_2$  at two extreme densities (see ESI).

In this work, the previously validated<sup>30</sup> methyldene phenalene (MPh) model (Scheme 1) was employed as the primary adsorbent “maquette”. A converging series of correlated molecular orbital (MO) levels of theory in conjunction with validated density functional theory (DFT) were used to describe the molecular geometry, interaction energies, and electronic structure of the  $H_2$  adsorption models. Our previous work is herein extended from  $CH_4$  to  $H_2$  physisorption with the aim of connecting molecular models to experimentally measured isosteric heats of adsorption on model porous carbon materials (e.g., on zeolite-templated carbon or on nanometer and larger pores of activated carbon, Scheme 1).

A representative depiction of a single-adsorption X-MPh $\times H_2$  model ( $X = B, C, \text{ or } N$ ) is shown in Figure 1. The metric parameters used to describe  $H_2$  adsorption are the angle of approach (end-on  $\varphi = 180^\circ$  to side-on  $\varphi = 90^\circ$  orientation), the tilt ( $\phi$ ) with respect to the site of substitution ( $X_1$ ), the distance between the  $H_2$  bond centroid ( $X_{H_2}$ ) and the nearest ring centroid ( $X_i$ ,  $X_{ii}$ , or  $X_{iii}$ ) of adsorption ( $d_i$ ,  $d_{ii}$ , or  $d_{iii}$ , respectively), the H–H bond distance of the adsorbed  $H_2$ , the distance from the proximal H to the relevant ring centroid ( $H_p \cdots X_i$ ), and the degree of deviation from centeredness of the  $H_2$  adsorbate from the nearest ring ( $\lambda$ ). Additional parameters used for describing the adsorbent are shown in Scheme S1.

The effects of heteroatom doping manifest to the greatest extent in the inner and the peripheral bond lengths (Table S4) of the adsorbent-only models (i.e., prior to  $H_2$  adsorption) consistent with past results on both periodic<sup>32</sup> and molecular<sup>22</sup> models. The C–N bonds in N-MPh are only slightly contracted (by 0.02 Å) as an evidence the lower structural impact of an added electron as compared to that for an added hole in the B-MPh models. The small variations in the outer atomic positions rationalize the use of the MPh model for capturing the effects

**Table 1:** Dissociation energies (in  $\text{kJ mol}^{-1}$ ) and entropies (expressed in multiples of the universal gas constant) for  $\text{MPh} \times nH_2 \rightarrow \text{MPh} + n H_2$  reaction obtained from MN15/6-311++G\*\* calculations. BSSE stands for basis set correction values. The condensed phase free energy ( $\Delta G_{\text{cond}}^\circ$ ) and entropy ( $\Delta S_{\text{cond}}^\circ$ ) values were estimated using free volume-based translational entropy correction<sup>15</sup> for  $H_2$  gas at 298 K, 1 bar, density 0.0813  $\text{g L}^{-1}$ .

Adsorbent	$n$	$\Delta E^{\text{QM}}$	BSSE	$\Delta H^\circ$	$\Delta G^\circ$	$\Delta G_{\text{cond}}^\circ$	$\Delta S_{\text{cond}}^\circ$
MPh	1	8	1	4	-17	-1	2
B-MPh	1	8	0	4	-17	0	2
N-MPh	1	8	1	4	-19	-3	3
MPh	2	17	2	8	-34	0	3
B-MPh	2	16	1	8	-34	0	3
N-MPh	2	17	2	9	-34	-1	3
MPh	6	54	6	28	-100	1	9
B-MPh	6	55	4	29	-107	-5	12
N-MPh	6	51	4	24	-114	-12	13
MPh	per $H_2$	$7.5 \pm 0.4$		$3.3 \pm 0.3$	$-17.7 \pm 0.9$	$-0.4 \pm 0.8$	$1.5 \pm 0.2$
B-MPh	per $H_2$	$7.9 \pm 0.5$		$3.7 \pm 0.4$	$-17.5 \pm 0.3$	$-0.4 \pm 0.4$	$1.7 \pm 0.3$
N-MPh	per $H_2$	$7.8 \pm 0.1$		$3.5 \pm 0.1$	$-18.9 \pm 0.8$	$-1.7 \pm 1.2$	$2.1 \pm 0.5$

of heteroatom substitution at a central graphitic site. The structures of the earlier adsorbent only models<sup>30, 33</sup> are similar to our adsorption models, as expected for physisorption.

In all calculations performed herein, the optimized position of any adsorbed  $H_2$  molecule is above one of the three aromatic rings (I, II, or III). Hence, a set of internal coordinates has been adopted that includes the distance between the H–H bond centroid ( $X_{H_2}$ ) and the corresponding ring centroid ( $X_i$ ), referred to as  $d_i$ , in addition to the associated angular orientations ( $\varphi$  and  $\phi$ , see Figure 1). The off-centeredness of the  $H_2$  molecule from the nearest ring center ( $\lambda$ ) is found to be dependent on the nature of the central atom ( $X_1$ ). The  $d_i$  distances show high similarity between the reference MPh and the electron-deficient B-MPh model (3.02–3.04 Å), but the electron-enriched N-MPh model pulls the  $H_2$  adsorbates considerably closer to its surface (2.83–2.98 Å) at low  $H_2$  loadings ( $n = 1$  and 2). The crowdedness of the N-MPh $\times 6H_2$  model results in close to 0.1 Å longer  $d_i$  distances with a significant standard deviation ( $\sigma = 0.17$  Å) compared to the N-MPh $\times H_2$  and N-MPh $\times 2H_2$  adsorption models ( $\sigma < 0.02$  Å).

A striking effect of heteroatom doping is the variation in  $\varphi$  that describes the end-on ( $180^\circ$ ) versus side-on ( $90^\circ$ ) orientation of  $H_2$ . In most of the N-MPh models, each  $H_2$  molecule interacts end-on ( $\phi = 85$ – $90^\circ$ ). In low loading MPh $\times nH_2$  and B-MPh $\times nH_2$  models with  $n = 1$  and 2, the adsorbed  $H_2$  molecules are similarly oriented  $\sim 10^\circ$  with respect to the end-on orientation, but the trends do not follow a pattern (Scheme S2). In the most saturated adsorption model (N-MPh $\times 6H_2$ ), the crowdedness and thus the significance of  $H_2 \cdots H_2$  interactions impact the preference for end-on/side-on interactions. Some models show side-on preference over the dominant end-on preference observed at low  $H_2$  loading. Furthermore, deviation from exact centeredness ( $\lambda$ ) is greatest for the electron-rich N-MPh models (0.15–0.21 Å, compared to 0.05–0.13 Å for MPh and B-MPh). In all cases herein, the H–H bonds are only slightly

**Table 2.** Dissociation energies (in  $\text{kJ mol}^{-1}$ ) for  $\text{MPh} \times n\text{H}_2 \rightarrow \text{MPh} + n\text{H}_2$  reaction obtained from the highest level DFT calculations (MN15+: MN15/def2QZVPP, BSSE  $< 1 \text{ kJ mol}^{-1}$ ) and conceptually converging *ab initio* wave function calculations using 6-311++G\*\* (BS1) and aug-cc-pVDZ (BS2) basis sets on MN15/6-311++G\*\* equilibrium structures. The modified CBS-QB3 calculations (mCBS-QB3) employed MN15 equilibrium geometries with only a single  $\text{H}_2$  adsorbate molecule. The significant basis set superposition errors (BSSE) from counterpoise calculation range from 10–14  $\text{kJ mol}^{-1}$  (B-MPh: 10.6 $\pm$ 0.6  $\text{kJ mol}^{-1}$ , MPh: 13.5 $\pm$ 0.8  $\text{kJ mol}^{-1}$ , N-MPh: 12.7 $\pm$ 0.7  $\text{kJ mol}^{-1}$ ) using BS1. The three bottom rows show an analysis per single  $\text{H}_2$  adsorbate of average energy values and their standard deviations.

Adsorbent	n	MN15+	MP2		MP3		MP4		CCSD(T)		mCBS-QB3
			BS1	BS2	BS1	BS2	BS1	BS2	BS1	BS2	
MPh	6	47	34	58	26	48	33	60	29	55	
B-MPh	6	51	19	41	15	37	21	46	27	47	
N-MPh	6	45	25	50	21	46	28	55	26	56	
MPh	per mol $\text{H}_2$	7.8	7.2 $\pm$ 1.3	9.7	5.6 $\pm$ 1.0	8.1	6.9 $\pm$ 1.1	9.9	5.1 $\pm$ 1.9	9.2	3.5 $\pm$ 0.2
B-MPh	per mol $\text{H}_2$	8.4	4.2 $\pm$ 0.9	6.9	3.4 $\pm$ 0.7	6.2	4.5 $\pm$ 0.7	7.7	5.5 $\pm$ 1.3	7.8	2.4 $\pm$ 0.4
N-MPh	per mol $\text{H}_2$	7.5	5.7 $\pm$ 1.3	8.3	4.7 $\pm$ 1.0	7.6	6.2 $\pm$ 1.3	9.2	6.2 $\pm$ 1.7	9.4	3.7 $\pm$ 0.2

elongated ( $< 0.02 \text{ \AA}$ ) relative to that of the free  $\text{H}_2$  molecule, which is a feature of physisorption.

In contrast to the case for  $\text{CH}_4$  physisorption on carbon surfaces,<sup>30</sup> this study reveals negligible energy differences ( $< 0.5 \text{ kJ mol}^{-1}$  per  $\text{H}_2$ ) among the heteroatom-substituted MPh adsorption models (Table 1). The reference level of DFT theory MN15/6-311++G\*\* (MN15),<sup>34–36</sup> used in both  $\text{CH}_4$  and  $\text{H}_2$  adsorption studies, yields an average BSSE-corrected<sup>37</sup> interaction energy for unsubstituted  $\text{MPh} \times n\text{H}_2$  of 7.5 $\pm$ 0.4  $\text{kJ mol}^{-1}$  on a per  $\text{H}_2$  basis. This is unexpected since the  $\text{H}_2$  binding distances ( $d_i$ ) are close to 0.2  $\text{Å}$  shorter in N-MPh $\times n\text{H}_2$  ( $n = 1$  and 2, see Table 2) than in MPh $\times n\text{H}_2$  or N-MPh $\times n\text{H}_2$ . The lack of energetic differences despite the significant geometric changes is rationalized by the comparable counteracting effect of the delocalization of an electron hole or excess electron in the  $\pi$ -system of X-MPh, polarizability of the adsorbent, and the competition of adsorbent-adsorbate and adsorbate-adsorbate interactions (*vide infra*). This lack of technologically relevant energetic differences among the B- and N-substituted models relative to the unsubstituted MPh suggests that energetic preference from experiments likely originates from the local structure of the adsorption site, not the chemical composition.

In order to confirm the negligible energy difference among the various adsorption site composition, the dissociation energies were further evaluated by correlated MO theory<sup>38</sup> (showing quite significant basis set effects), and the complete basis set extrapolation scheme<sup>39, 40</sup> (a modified CBS-QB3 method using MN15 geometries for X-MPh $\times \text{H}_2$  models only, mCBS-QB3, Table 2). The use of a more complete basis set (def2QZVPP<sup>41, 42</sup> in MN15+) with negligible BSSE results in the same desorption energy values as MN15 with BSSE correction for six  $\text{H}_2$  molecules. The binding energy difference per  $\text{H}_2$  molecule at the MN15+ level remains within 1  $\text{kJ mol}^{-1}$  with a technologically insignificant preference with respect to  $\text{H}_2$  binding for B over C or N (8.4, 7.8, and 7.5, respectively, Table 2). In parallel, the binding energy differences from the MO theory calculations MP2-MP4 series<sup>43–45</sup> to CCSD(T)<sup>46–48</sup> gradually diminishes. At the CCSD(T)/aug-cc-pVDZ<sup>49, 50</sup> and the mCBS-QB3 levels, the heteroatom-substituted models show only slightly stronger interaction from the unsubstituted model. It is worth highlighting that the mCBS-QB3 values correspond purely to the adsorbent/adsorbate interaction, while the CCSD(T) values contain also the adsorbate/adsorbate interaction energies.

The combinatorial mapping of positional isomers for adsorption models (X-MPh $\times n\text{H}_2$ ,  $n = 1–6$  and X = C, B, or N, Scheme S2) provides a finer grain view of the energy landscape, since in high surface area porous carbon materials, the  $\text{H}_2$  can access both sides of each hydrocarbon fragment (see Scheme 1). The  $n = 1$  models show a tight grouping of BSSE-corrected interaction energies of  $\Delta E^{\text{QM}*} = 7.4 \pm 0.4 \text{ kJ mol}^{-1}$ . This increases to 14.8 $\pm$ 0.7  $\text{kJ mol}^{-1}$  for the  $n = 2$  models (12.9–15.8  $\text{kJ mol}^{-1}$ ). The  $n = 3$  models exhibit similar energetic variations (22.7 $\pm$ 1.0  $\text{kJ mol}^{-1}$  within a wider range of 21.3–26.0  $\text{kJ mol}^{-1}$ ) as the influence of  $\text{H}_2$  cooperativity emerges. The upper limit of the range of interaction energies becomes greater than the sum of the adsorbent-adsorbate interactions. For models with high  $\text{H}_2$  loading ( $n = 4, 5$ , and 6), the crowdedness of adsorbate molecules increases, which further increases the standard deviation of the average interaction energies (30.6 $\pm$ 1.7, 39.5 $\pm$ 1.6, and 48.7 $\pm$ 2.3  $\text{kJ mol}^{-1}$  within ranges of 26.0–33.4, 36.5–41.3, and 46.7–51.2  $\text{kJ mol}^{-1}$ , for 4, 5, and 6 adsorbates, respectively). The range widens despite that the number of positional isomers decreases as loading increases (Scheme S2, Figure S3). Cooperativity is most evident in the highly loaded, B-MPh $\times 6\text{H}_2$  model, since the adsorption energy ( $\Delta E^{\text{QM}*} = 8.1 \text{ kJ mol}^{-1}$  per  $\text{H}_2$  molecule) is greater than in the MPh $\times \text{H}_2$  models ( $\Delta E^{\text{QM}*} = 7.4 \text{ kJ mol}^{-1}$ ). The increased binding energy can be attributed to  $\text{H}_2 \cdots \text{H}_2$  interactions that are calculated to be 4.2–4.5  $\text{kJ mol}^{-1}$  for the 6  $\text{H}_2$  molecules, approximately evenly distributed (2.1–2.5 and 2.1–2.0  $\text{kJ mol}^{-1}$ ) for the 3  $\text{H}_2$  molecules above and below the MPh adsorbent plane. The graphical depiction of the spread of energies among the positional isomers (Figure S3, using the experimentally relevant adsorption energy formalism, *vide infra*) reveals that the energetic preference for the strongest adsorbent/adsorbate interaction may vary in a non-trivial way as a function of  $\text{H}_2$  loading. While the N-MPh system was predicted to correspond to the strongest binding energies at low  $\text{H}_2$  uptake (Figure S4a), exceptions arise including the maximum loading ( $n = 6$ ) model, where adsorption on B-MPh becomes energetically most favorable (Figure S4b).

To gain insights into the origins of the unexpected trends, the electron density differences among the adsorption models and the non-interacting (isolated) adsorbent and adsorbate molecules are shown in Figure 2. At the same isocontour level, the B-MPh $\times 6\text{H}_2$  model shows the largest electron density differences (Figure 2b), and a well defined orientation of the

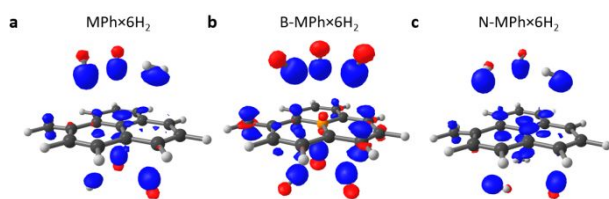


**Figure 2.** Electron density difference between the adsorption model X-MPh $\times$ 6H $_2$  (X = C, B, or N) and the isolated X-MPh adsorbent and 6 H $_2$  adsorbate molecules at an isocontour value of 0.005 ( $e^-$ )  $\text{\AA}^3$ , calculated at the MN15+ level of theory (MN15/def2-QZVPP). The exclusively end-on orientation of the H $_2$  molecules in B-MPh $\times$ 6H $_2$  contrasts the mixed end-on and side-on orientation for the unsubstituted and the N-substituted adsorption models.

electron density different contours that correspond to the strongest induced electrostatic interactions. In contrast to the electron density differences, no significant ( $>0.01 e^-$ ) differences were calculated in the electron density ( $q(6H_2) = -0.10 - -0.11 e^-$ ) and spin density ( $\rho(6H_2) = 0.01 - 0.02 e^-$ ) accumulated on the 6 H $_2$  adsorbates of the adsorption models from Hirshfeld population analysis.<sup>51</sup> The electronic structural features in Figure 2b indicate that the presence of an electron hole in the conjugated  $\pi$ -system upon B-doping focuses the polarization of the end-on coordinated adsorbent H $_2$  molecules toward the B-substituted central site. On the other hand, for both MPh and N-MPh, the orientations of the adsorbates are mixed end-on and side-on due to a more electron rich environment than in B-MPh.

In order to further evaluate the lack of significant energetic variations among the physisorption of H $_2$  on the unsubstituted and the B- or N-doped site of substitution, we considered an expanded model of MPh (pbaMPh) and a curved maquette with blade-like morphology at low and high H $_2$  loading. The optimized structures of these large, more realistic maquettes with surface curvature and significant H $_2$  crowding are shown in Figures S5 and S6. Without exception, all of the models show dissociation energies that are within 1.1 kJ mol $^{-1}$  for the the three compositions (Table S5). An additional set of models were created using the curved blade adsorbent model in a 9 $\times$ 17 $\times$ 24  $\text{\AA}$  boundary box with H $_2$  loading corresponding to two density extremes (33 and 84 H $_2$  molecules per blade) of liquid H $_2$  (Figure S6). The latter high-coverage models exhibit, on average, 7 kJ mol $^{-1}$  interaction energies ( $\Delta E^{\text{QM}}$  per H $_2$  molecule) in comparison to the simpler maquettes that all consistently show around 10 kJ mol $^{-1}$  per H $_2$ , regardless of the size or the coverage of the model.

The experimentally relevant quantity describing the strength of interaction between H $_2$  and the surface of a material is the isosteric heat of adsorption ( $q_{\text{st}}$ ). At constant pressure,  $q_{\text{st}}$  is equivalent to the enthalpy of adsorption.<sup>52</sup> This quantity can be experimentally determined by the isosteric method.<sup>53, 54</sup> Measurements of hydrogen adsorption equilibria on a wide diversity of carbon materials show that the heat of adsorption varies from 4–8 kJ mol $^{-1}$ , depending on the pore size.<sup>55</sup> Representative previous measurements<sup>4</sup> and our current results reported herein (Figure S7) are summarized in Figure S8. ZTC was chosen as a model adsorbent since it contains exclusively two-sided, graphene-like nanoribbons

with copious edge sites and a wide enough pore diameter (1.2 nm) to preclude any role for confinement effects.<sup>10</sup> The isosteric heat of H $_2$  adsorption on ZTC was found to be 4.1–4.6 kJ mol $^{-1}$  at room temperature when described by a dual-site Langmuir model (Table S6). Measurements up to higher pressures<sup>4</sup> show that it remains relatively constant between sparse loadings and up to 20 mmol g $^{-1}$ , roughly corresponding to 3.5 H $_2$  per MPh equivalents. Following the same analysis as previously used for methane,<sup>30</sup> first-principle calculations of adsorbate-adsorbent interactions can be best compared with experimental results by using a combination of the BSSE-corrected<sup>37</sup> potential energy ( $E^{\text{QM}*}$ ), the zero-point correction ( $E_{\text{ZPE}}$ ), and the addition of the  $\Delta(\text{PV})$  term (well approximated herein as RT given the ideality of H $_2$  in this loading range) to convert from energy to  $q_{\text{st}}$ . This comparison is shown in Figure S8, demonstrating consistency within the error ascribed to the calculations presented herein. It is remarkable that the same “quantum mechanics to thermodynamics” conversion previously validated for methane adsorption<sup>30</sup> also represents the closest match to experimental data in the case of hydrogen adsorption, stated as  $\Delta E^{\text{QM}*} + \Delta E_{\text{ZPE}} + \Delta \text{PV} \approx \Delta H_{\text{exp}}$ .

In conclusion, this work has extended our previous methane adsorption study to hydrogen by using rationally designed molecular maquettes representing the open surfaces of high surface area, porous carbon-based materials. For methane storage and delivery, a technologically relevant difference between N-doped and unsubstituted or B-doped systems was estimated ( $\Delta(\Delta E_{\text{ads}}) = 4\text{--}6$  kJ mol $^{-1}$ ). On the other hand, no evidence for significant preference ( $\Delta(\Delta E_{\text{ads}}) < 1$  kJ mol $^{-1}$ ) was found for hydrogen physisorption. Methane adsorption involves three rings per adsorbate due to the C-H $\cdots\pi$  hydrogen bonding and tetrel bonding with the central site of adsorption. On the contrary, hydrogen adsorption is localized at the center of a single ring for each adsorbate molecule, in a random orientation between end-on or side-on interaction, where a single heteroatom substitution of a site within a ring has a diminished effect on the binding energy. However, the H $_2$  adsorbate/adsorbent interaction is far from a simple H $_2\cdots\pi$  interaction. A detailed look at the interaction energies as a function of hydrogen loading suggests the existence of a non-trivial energetic preference for various binding sites and compositions as a function of the number of hydrogen adsorbates. These observations were further substantiated using expanded models with and without realistic curvatures. The computational results presented herein also suggest the presence of cooperative effects among adsorbent/adsorbate and adsorbate/adsorbate interactions that are of comparable interaction energies. The interplay of electronic and geometric structural features, morphologies, adsorbate/adsorbate interactions, and related energetics does not allow for broad generalization, which can be deconvoluted by employing realistic computational models at the highest level of theory accessible to derive design principles for next-generation hydrogen storage materials.

## Conflicts of interest

There are no conflicts to declare.

## Author contributions

Rylan Rowsey, Erin Taylor, and Ryan Hinson performed computational investigations, formal analysis, and methodology development; Dalton Compton carried out the experimental measurements and formal analysis; Nicholas Stadie and Robert Szilagyí conceptualized and administered the project, supervised the investigations, and wrote the manuscript with assistance from all of the co-authors.

## Acknowledgements:

This work is supported by the U.S. Department of Energy's Office of Energy Efficiency and Renewable Energy (EERE) under the Hydrogen and Fuel Cell Technologies and Vehicle Technologies Offices (award number DE-EE0008815). We are also grateful for resources provided by the Extreme Science and Engineering Discovery Environment (XSEDE, supported by National Science Foundation grant ACI-1548562). We acknowledge access to the Hyalite High Performance Computing System, operated and supported by the University Information Technology Research Cyberinfrastructure at Montana State University. This research was also supported in part through computational resources and services provided by Advanced Research Computing at the University of British Columbia and Digital Research Alliance of Canada (RRG #4177).

## Notes and references

- 1 Y. D. Xia, Z. X. Yang and Y. Q. Zhu, *J. Mater. Chem. A*, 2013, **1**, 9365-9381.
- 2 W. C. Xu, K. Takahashi, Y. Matsuo, Y. Hattori, M. Kumagai, S. Ishiyama, K. Kaneko and S. Iijima, *Int. J. Hydrog. Energy*, 2007, **32**, 2504-2512.
- 3 M. Hirscher and B. Panella, *Scr. Mater.*, 2007, **56**, 809-812.
- 4 N. P. Stadie, J. J. Vajo, R. W. Cumberland, A. A. Wilson, C. C. Ahn and B. Fultz, *Langmuir*, 2012, **28**, 10057-10063.
- 5 H. Nishihara, P.-X. Hou, L.-X. Li, M. Ito, M. Uchiyama, T. Kaburagi, A. Ikura, J. Katamura, T. Kawarada, K. Mizuuchi and T. Kyotani, *Journal of Physical Chemistry C*, 2009, **113**, 3189-3196.
- 6 Y. D. Xia, G. S. Walker, D. M. Grant and R. Mokaya, *J. Am. Chem. Soc.*, 2009, **131**, 16493-16499.
- 7 N. Shcherban, S. Filonenko, P. Yaremov, V. Dyadyun, I. Bezverkhy and V. Ilyin, *J. Mater. Sci.*, 2017, **52**, 1523-1533.
- 8 X. B. Zhao, B. Xiao, A. J. Fletcher and K. M. Thomas, *J. Phys. Chem. B*, 2005, **109**, 8880-8888.
- 9 J. Purewal, D. G. Liu, A. Sudik, M. Veenstra, J. Yang, S. Maurer, U. Muller and D. J. Siegel, *Journal of Physical Chemistry C*, 2012, **116**, 20199-20212.
- 10 H. Nishihara and T. Kyotani, *Chemical Communications*, 2018, **54**, 5648-5673.
- 11 T. X. Nguyen, N. Cohaut, J. S. Bae and S. K. Bhatia, *Langmuir*, 2008, **24**, 7912-7922.
- 12 Z. Jin, Z. Z. Sun, L. J. Simpson, K. J. O'Neill, P. A. Parilla, Y. Li, N. P. Stadie, C. C. Ahn, C. Kittrell and J. M. Tour, *J. Am. Chem. Soc.*, 2010, **132**, 15246-15251.
- 13 Y. Jeong and T. C. M. Chung, *Carbon*, 2010, **48**, 2526-2537.
- 14 T. C. M. Chung, Y. Jeong, Q. Chen, A. Kleinhammes and Y. Wu, *J. Am. Chem. Soc.*, 2008, **130**, 6668-+.
- 15 M. Mammen, E. I. Shakhnovich and G. M. Whitesides, *Journal of Organic Chemistry*, 1998, **63**, 3168-3175.
- 16 D. P. Broom and M. Hirscher, *Energy Environ. Sci.*, 2016, **9**, 3368-3380.
- 17 I. Cabria, M. J. Lopez and J. A. Alonso, *J. Chem. Phys.*, 2017, **146**, 11.
- 18 M. Bin Yeamin, N. Faginas-Lago, M. Alberti, I. G. Cuesta, J. Sanchez-Marin and A. de Meras, *RSC Adv.*, 2014, **4**, 54447-54453.
- 19 J. Ma, A. Michaelides and D. Alfe, *J. Chem. Phys.*, 2011, **134**, 6.
- 20 L. Firlej, S. Roszak, B. Kuchta, P. Pfeifer and C. Wexler, *J. Chem. Phys.*, 2009, **131**, 4.
- 21 Z. Zhou, X. P. Gao, J. Yan and D. Y. Song, *Carbon*, 2006, **44**, 939-947.
- 22 I. Nayyar, B. Ginovska, A. Karkamkar, T. Gennett and T. Autrey, *C - J. Carbon. Res.*, 2020, **6**.
- 23 E. Varenus, Chalmers University of Technology, 2011.
- 24 J. Y. Dai, J. M. Yuan and P. Giannozzi, *Appl. Phys. Lett.*, 2009, **95**, 3.
- 25 Z. H. Zhu, H. Hatori, S. B. Wang and G. Q. Lu, *J. Phys. Chem. B*, 2005, **109**, 16744-16749.
- 26 Y. Ferro, F. Marinelli, A. Jelea and A. Allouche, *J. Chem. Phys.*, 2004, **120**, 11882-11888.
- 27 Y. Ferro, F. Marinelli, A. Allouche and C. Brosset, *J. Chem. Phys.*, 2003, **118**, 5650-5657.
- 28 X. Sha, A. C. Cooper, W. H. Bailey, III and H. Cheng, *Journal of Physical Chemistry C*, 2010, **114**, 3260-3264.
- 29 C. Zhang and A. Alavi, *J. Chem. Phys.*, 2007, **127**.
- 30 R. Rowsey, E. E. Taylor, S. Irle, N. P. Stadie and R. K. Szilagyí, *J. Phys. Chem. A*, 2021, **125**, 6042-6058.
- 31 L. Wang, Z. Sofer and M. Pumera, *ACS Nano*, 2020, **14**, 21-25.
- 32 Z. Zhang and K. Cho, *Phys. Rev. B*, 2007, **75**.
- 33 R. K. Szilagyí and R. Rowsey, in *ZENODO 4898710*, 2021.
- 34 H. Y. S. Yu, X. He, S. H. L. Li and D. G. Truhlar, *Chem. Sci.*, 2016, **7**, 5032-5051.
- 35 M. J. Frisch, J. A. Pople and J. S. Binkley, *J. Chem. Phys.*, 1984, **80**, 3265-3269.
- 36 R. Krishnan, J. S. Binkley, R. Seeger and J. A. Pople, *J. Chem. Phys.*, 1980, **72**, 650-654.
- 37 L. A. Burns, M. S. Marshall and C. D. Sherrill, *Journal of Chemical Theory and Computation*, 2014, **10**, 49-57.
- 38 J. A. Pople, *Reviews of Modern Physics*, 1999, **71**, 1267-1274.
- 39 J. A. Montgomery, M. J. Frisch, J. W. Ochterski and G. A. Petersson, *J. Chem. Phys.*, 2000, **112**, 6532-6542.
- 40 J. A. Montgomery, M. J. Frisch, J. W. Ochterski and G. A. Petersson, *J. Chem. Phys.*, 1999, **110**, 2822-2827.
- 41 F. Weigend, *Phys. Chem. Chem. Phys.*, 2006, **8**, 1057-1065.
- 42 F. Weigend and R. Ahlrichs, *Phys. Chem. Chem. Phys.*, 2005, **7**, 3297-3305.
- 43 M. J. Frisch, M. Head-Gordon and J. A. Pople, *Chem. Phys. Lett.*, 1990, **166**, 275-280.
- 44 J. A. Pople, J. S. Binkley and R. Seeger, *Int. J. Quantum Chem.*, 1976, 1-19.
- 45 R. Krishnan and J. A. Pople, *Int. J. Quantum Chem.*, 1978, **14**, 91-100.
- 46 G. D. Purvis and R. J. Bartlett, *J. Chem. Phys.*, 1982, **76**, 1910-1918.
- 47 G. E. Scuseria, C. L. Janssen and H. F. Schaefer, *J. Chem. Phys.*, 1988, **89**, 7382-7387.

## COMMUNICATION

## PCCP

- 48 J. A. Pople, M. Headgordon and K. Raghavachari, *J. Chem. Phys.*, 1987, **87**, 5968-5975.
- 49 E. R. Davidson, *Chem. Phys. Lett.*, 1996, **260**, 514-518.
- 50 R. A. Kendall, T. H. Dunning and R. J. Harrison, *J. Chem. Phys.*, 1992, **96**, 6796-6806.
- 51 F. L. Hirshfeld, *Theor. Chim. Acta*, 1977, **44**, 129-138.
- 52 N. P. Stadie, Ph.D. Dissertation, California Institute of Technology, 2013.
- 53 A. F. Kloutse, R. Zacharia, D. Cossement, R. Chahine, R. Balderas-Xicohtencatl, H. Oh, B. Streppel, M. Schlichtenmayer and M. Hirscher, *Appl. Phys. A-Mater. Sci. Process.*, 2015, **121**, 1417-1424.
- 54 D. Shen, M. Bülow, F. Siperstein, M. Engelhard and A. L. Myers, *Adsorption*, 2000, **6**, 275-286.
- 55 A. Gigras, S. K. Bhatia, A. V. A. Kumar and A. L. Myers, *Carbon*, 2007, **45**, 1043-1050.